# High-throughput synthesis of core–shell and multi-shelled materials by fluidised bed chemical vapour deposition. Case study: double-shell rutile–anatase particles

M. J. Powell, R. Quesada-Cabrera, W. L. Travis and I. P. Parkin*

Fluidised Bed Chemical Vapour Deposition (FBCVD) has been widely used for the industrial production of corrosion resistant and mechanically robust coatings. Laboratory-based FBCVD rigs are less common, however, this technique is ideal for the high-throughput production of core–shell and multi-shelled materials, allowing large areas to be coated in a fast and cost effective way. The method is also convenient for the optimisation of advanced materials with tuned structural, electronic and functional properties. In this work, the synthesis of double-shelled rutile–anatase $TiO_2$ particles is presented as a case study. Electron transfer mechanisms at the junction level of the two polymorphs have been reported as responsible for the high efficiency of $TiO_2$-based materials, such as the well-known Evonik P25 standard. The photocatalytic performance of the double-shelled particles was evaluated during the mineralisation of a model organic pollutant (stearic acid) and compared with that of the individual components. To the best of our knowledge, this is the first time that multi-shelled particles have been synthesised from a chemical vapour deposition route.

## Introduction

In recent years, a wide range of advanced core–shell and multi-shelled materials have been successfully used as anti-microbial[1–3] and medical treatment systems,[4–6] photocatalysts,[7–9] thermochromic materials,[10–12] quantum dots[13–15] and battery compounds.[16–19] These multi-component systems take advantage of the synergistic interaction between different layers (electron transfer processes, lattice matching, *etc.*) to suit particular functional properties. For instance, there have been many reports on core–shell arrays for use as high performance capacitance materials.[19–22] Core–shell particles have also been reported for their excellent photonic properties.[13,23,24] Unfortunately, the main techniques reported for the synthesis of core–shell and multi-shelled materials are currently solution based, which can be undesirable for industrial scale-up production due to the long reaction times (3–4 days), expensive solvents, refining of the product and batch-like nature of the reactions. Thus, an alternative scalable approach is crucial for the introduction of these advanced materials into the market.

Chemical Vapour Deposition (CVD) techniques are favoured in many industrial processes due to fast growth rates, ease of scaling and 'on-line' production.[25–27] CVD has been widely used in the synthesis of coatings and thin films, including well-known examples such as the self-cleaning glass developed by Pilkington©, which contains a very thin layer of titanium dioxide ($TiO_2$).[28] This paper introduces a versatile, lab-scale fluidised bed chemical vapour deposition (FBCVD) system that allows large areas of samples in powder form to be uniformly coated with highly-crystalline, robust films. This method has been used industrially to apply corrosion resistant and mechanically robust coatings, such as titanium carbide,[29] silicon carbide[30] and aluminide coatings[31] on powders and it has also been employed for the synthesis of carbon nanotubes.[32]

FBCVD permits the synthesis of films onto powder supports by the heating and fluidisation of the powder support followed by chemical vapour deposition (by volatile precursors) of the desired material on top of the powder. The FBCVD system affords control of film growth rate and the high-throughput synthesis of advanced (doped) core–shell and multi-shelled compounds. The synthesis and photocatalytic properties of multi-shelled rutile@anatase titania ($TiO_2$) coatings on mica substrates were investigated here as a case study, along with mixed phase anatase and rutile shells and the individual components. This has allowed us to test the widely held view that vectorial electron charge separation and consequent increase in photogenerated charge lifetimes are responsible for the enhanced activity observed in rutile–anatase materials under UV illumination.[33–35]

Multi-shell systems such as the case study introduced here are of increasing interest.[36,37] A CVD approach allows successive

*University College London, Department of Chemistry, Materials Chemistry Centre, 20 Gordon St., London WC1H 0AJ, UK. E-mail: i.p.parkin@ucl.ac.uk*

shells to be deposited and the samples can be coated as many times as it is required. The thickness of each layer and concentration of dopants can be carefully tailored to achieve the desired properties in the final product. In the case of core–shell particles, there have been many reports on the synthesis of Au@$SiO_2$ core–shell materials,[38–40] which typically involve aqueous routes. This is a relatively slow process and is not easily scalable for industrial applications. Again in the latter case, CVD offers a convenient way to dope both the core and shells of such a structure,[41–44] with the ability to control the dopant level by the concentration of the dopant in the precursor mix.

# Experimental

### Chemical precursors

Titanium(IV) chloride ($TiCl_4$, 99.9%) and ethyl acetate anhydrous ($C_4H_8O_2$, 99.8%) was purchased from Sigma Aldrich UK. Mica (Symic C001, synthetic fluorphlogopite : $TiO_2$ 80 : 20) was purchased from Eckert, the particle size range was 10–40 μm. All chemicals/substrates were used as received with no additional workup. Oxygen-free nitrogen (99.9%) was purchased from BOC. Octadecanoic (stearic) acid was purchased from Sigma Aldrich ($CH_3(CH_2)_{16}COOH$, ≥95%).

### The fluidised bed CVD apparatus

The samples were produced using a specially designed hot-walled Fluidised Bed Chemical Vapour Deposition (FBCVD) reactor. Fig. 1(a) and (b) shows a schematic design of the FBCVD rig and a photograph of the system. The precursors were contained in stainless steel cylinders (bubblers) with brass jackets and heating bands. Nitrogen ($N_2$) was used as a carrier gas. All the stainless steel lines were heated using heating tapes (Electrothermal 400 W, 230 V) and the temperature of all the components of the rig controlled using k-type thermocouples with Thermotron controllers. The precursors were pre-mixed in a stainless steel mixing chamber. The hot-walled reaction chamber was created using a tube furnace, fitted with a Eurotherm controller. Fluidisation of the mica support was achieved by carrier gas flow only (Fig. 1(c)). The design presented here is a fixed bed; there are no moving parts within the reactor. In general, fluidisation occurred at flow rates above ~7 L $min^{-1}$ but total flow rates of >10 L $min^{-1}$ are typically used to ensure complete fluidisation of the particles. Stainless steel gauzes (diameter size: 0.1 mm) are placed at the two ends of the reactor in order to prevent excess mica escaping the reaction chamber during deposition.

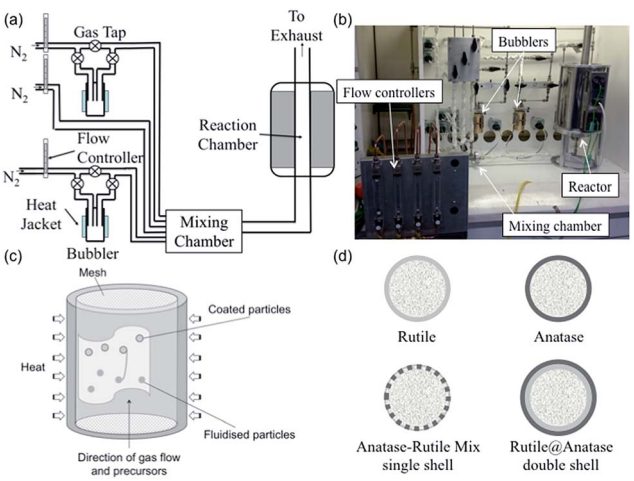


Fig. 1 (a) Schematic design of the Fluidised Bed Chemical Vapour Deposition (FBCVD) system. (b) Photograph of the FBCVD system at UCL (c) diagram showing the fluidisation process of the particles in the FBCVD reactor; (d) schematic representation of the rutile–anatase single-shelled and double-shelled coatings and the pure components investigated here.

### Synthesis of double-shelled $TiO_2$ materials

Titanium dioxide ($TiO_2$) was deposited from reaction of titanium chloride ($TiCl_4$) and ethyl acetate ($C_4H_8O_2$),[45] as described in eqn (1), on ~3 g of mica under the conditions described in Table 1. The temperature ramp rate of the reactor was 20 °C $min^{-1}$ and it was kept at the target temperature for at least 30 min before deposition. The $TiCl_4$ and $C_4H_8O_2$ bubblers were set to 75 and 40 °C, respectively.

The plain nitrogen flow rate was set to 10 L $min^{-1}$ and the corresponding flow rates for $TiCl_4$ and $C_4H_8O_2$ were both set to 0.6 L $min^{-1}$. The deposition time for each sample was 30 min. After the deposition, the reactor was left to cool under nitrogen flow. All samples were post annealed in a furnace (ramp rate 20 °C $min^{-1}$) for 10 h to enhance crystallinity. The $TiO_2$ coating is deposited as pure anatase phase at 500 °C and as anatase–rutile mixture at 750 °C. The rutile $TiO_2$ layers were formed from the anatase phase at 1000 °C in air. For the double-shelled rutile@anatase sample, the powder was transferred back to the FBCVD reactor after the formation of the rutile layer and an anatase layer was then deposited at 500 °C. The latter sample was post-annealed again at 500 °C for 10 h. A schematic representation of the different coatings produced for this work is shown in Fig. 1(d).

$$TiCl_4\ (g) + CH_3COOC_2H_5\ (g) \rightarrow TiO_2 + \text{byproducts} \quad (1)$$

### Film characterisation

X-ray diffraction (XRD) studies were carried out using a *Stoe* (Mo) *StaniP* diffractometer. The instrument operates with a Mo X-ray source (Mo tube 50 kV 30 mA), monochromated (Pre-sample Ge (111) monochromator selects Kα1 only) and a *Dectris Mython* 1k silicon strip detector covering 18° ($2\theta$). Samples were run in transmission mode, with the sample being rotated in the X-ray beam. The diffraction patterns obtained were compared with database standards. Raman spectroscopy was carried out using a *Renishaw 1000* spectrometer equipped with a 633 nm laser. The Raman system was calibrated using a silicon reference. UV/vis spectroscopy was performed using a *Perkin Elmer Lambda 950* UV/Vis/NIR Spectrophotometer. The absorption spectra were recorded *via* diffuse reflectance, with the samples being deposited onto microscope slides. A *Labsphere* reflectance

Table 1 Synthesis conditions and surface areas of single- and double-shelled $TiO_2$ samples on mica support

| | | Deposition conditions | | Annealing conditions | | | | | |
|---|---|---|---|---|---|---|---|---|---|
| Name | Description | Time (min) | $T$ (°C) | $T$ (°C) | Time (h) | Size (nm) | $S_{BET}$ ($m^2\ g^{-1}$) | $E_g$ (eV) | $\xi$ (molec photon$^{-1}$) $\times 10^{-6}$ |
| Anatase | Anatase | 30 | 500 | 500 | 10 | 65 | 5 | 3.11 | 48.4 |
| Anatase–rutile | Single-shelled mix | 30 | 750 | 750 | 10 | 60 | 12 | 3.10 | 23.6 |
| Rutile | Rutile | 30 | 500 | 1000 | 10 | 58 | 5 | 2.84 | 2.1 |
| Rutile@anatase | Double-shelled | 30 | 500 | 1000 | 10 | 63 | 3 | 2.90 | 12.7 |
| | (Anatase on rutile) | 30 | 500 | 500 | 10 | | | | |

standard was used as reference in the UV/vis measurements. Transmission electron microscopy (TEM) images were obtained using a TEM *Jeol* 2100 with a $LaB_6$ source operating at an acceleration voltage of 100 kV. Micrographs were recorded on a *Gatan Orius* charge-coupled device (CCD). The powders were sonicated and suspended in methanol and drop-casted onto a 400 Cu mesh lacey carbon film grid (*Agar Scientific Ltd.*) for TEM analysis. Low-temperature nitrogen adsorption–desorption isotherms were measured at 77 K using a *Quantachrome Autosorb-IQ2* machine. Specific surface area was measured using the desorption isotherm within relative pressures of 0.01 and 0.3, in accordance with the Brunauer–Emmett–Teller (BET) method.

### Photocatalytic testing

For the evaluation of their photocatalytic activity, the samples were dip-coated onto borosilicate glass slides from 1 wt% aqueous solutions. The immersion time was 10 s and withdrawal of 30 cm $min^{-1}$ during the dip coating process. The samples were then dried overnight at 100 °C. A layer of stearic acid was drop-casted onto the samples from a chloroform solution (0.05 M). The degradation of the acid was monitored by infrared spectroscopy (2700–3000 $cm^{-1}$) using a *Perkin Elmer RX-I* Fourier transform infrared spectrometer. The samples were irradiated in a home-built light box equipped with six blacklight blue fluorescent tubes (UVA 6 × 18 W) and an extractor fan. The irradiance ($4 \pm 0.2$ mW $cm^{-2}$) at sample position was measured using a *UVX* radiometer (*UVP*). The area of the sample under illumination was 3.14 $cm^2$.

## Results and discussion

### Physical and optical characterisation

A series of double-shelled rutile@anatase, single-shelled anatase–rutile mix and individual pure anatase and rutile coatings were deposited on mica particles by *Fluidised Bed* Chemical Vapour Deposition (FBCVD). The $TiO_2$ films were synthesised by reaction between $TiCl_4$ and ethyl acetate as described above (*vide supra*).

The as-deposited pure anatase $TiO_2$ films were transparent and thus looked greyish on the mica substrate, which was originally of white/silvery colour. On the contrary, the powders annealed at 750 and 1000 °C, which contained the rutile phase, had a golden/cream colour.

Diffuse reflection UV/vis spectra (Fig. 2) showed a red-shift of the absorption spectra for those samples containing the rutile phase, in agreement with the literature.[46] Close inspection of Fig. 2 suggests that the single-shelled anatase–rutile mix sample was predominantly anatase, since the absorption spectrum of the former is similar to that of pure anatase $TiO_2$, whilst the double-shelled rutile@anatase material had a clear rutile component. Tauc plots[43,47] were calculated from absorbance data in order to estimate the corresponding band-gap energies of these materials (Fig. 2, inset). The pure anatase and rutile phases had band-gap energies of 3.11 and 2.84 eV, respectively, which are lower than literature values.[48,49] As expected, the mix and double-shelled rutile@anatase samples showed band-gap energies within these two extreme values (3.10 and 2.90 eV, respectively).

XRD analysis confirmed the presence of pure crystalline anatase and rutile $TiO_2$ phases (Fig. 3(a)). The individual rutile and anatase samples were compared to standard samples (ICSD database) and the additional peaks observed in the patterns were due to the mica substrate. The intensity and sharpness of the diffraction peaks are in contrast with the typical broadening observed in XRD patterns of CVD $TiO_2$ thin films.[27] The single-

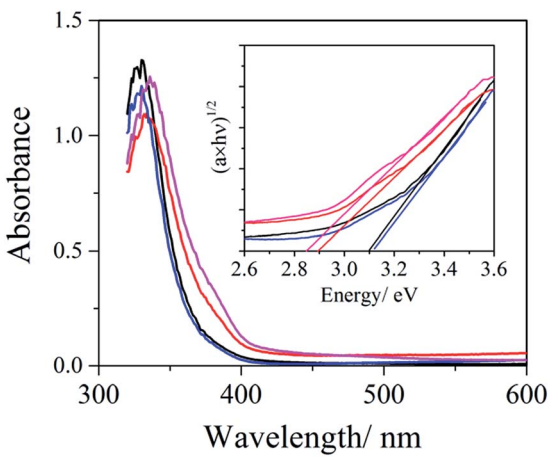


Fig. 2 Diffuse reflectance spectra of typical double-shelled rutile@anatase (red line), single-shelled rutile–anatase mix (black line) and pure anatase (blue line) and rutile (pink line) materials. Inset, corresponding Tauc plots showing band-gap energies for these samples line colours match description above.

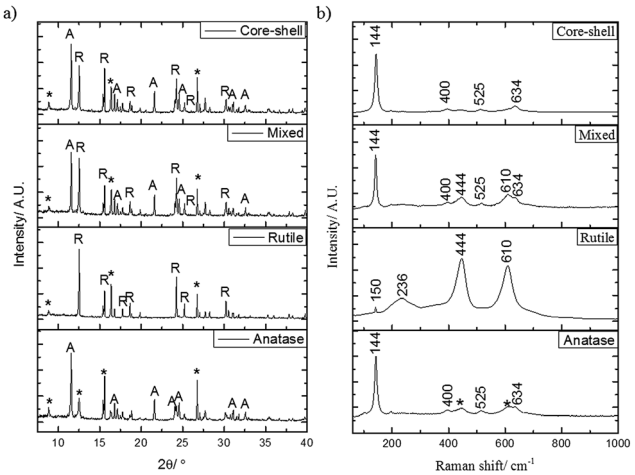


Fig. 3 (a) XRD patterns of pure anatase and rutile $TiO_2$ layers, single-shelled anatase–rutile mix and double-shelled rutile@anatase materials. Anatase peaks are denoted by (A), rutile peaks are denoted by (R) and the mica substrate peaks are denoted by (*). (b) Corresponding Raman spectra with rutile and anatase bands assigned. Mica bands denoted by (*) symbols.

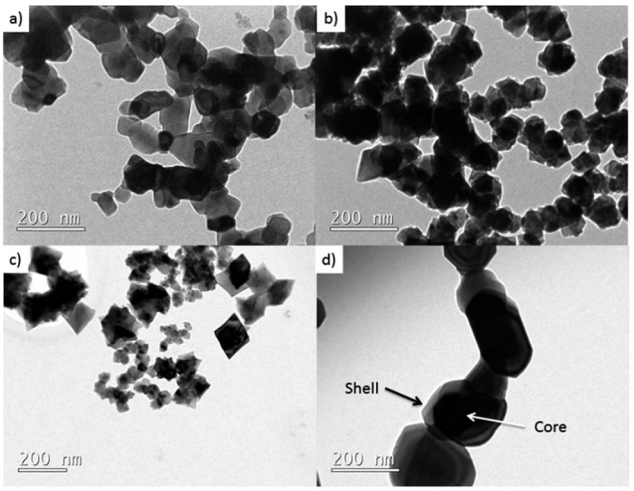


Fig. 4 Transmission Electron Microscopy (TEM) images from (a) anatase $TiO_2$; (b) rutile $TiO_2$; (c) single-shelled anatase–rutile $TiO_2$ mix and (d) double-shelled rutile@anatase $TiO_2$ particles.

shelled mix and double-shelled samples showed the presence of both anatase and rutile phases. Surprisingly, the XRD pattern of the single-shelled mix sample (Fig. 3(a)) showed similar peak intensity ratios of the two polymorphs, which was unexpected considering that the absorption properties of this sample were similar to pure anatase (Fig. 2).

The crystallite size in the samples was roughly estimated using the Scherrer equation within the range of 58–65 nm.

Further structural studies were carried out using Raman spectroscopy (Fig. 3(b)). Consistent with the XRD results, the pure anatase and rutile samples showed bands associated with these phases,[50] and no impurity phases were identified. The characteristic Raman-active modes of the anatase $TiO_2$ structure were observed at 144, 197, 634 ($E_g$), 525 ($A_{1g} + B_{1g}$) and 400 ($B_{1g}$) $cm^{-1}$.[50] Some additional bands were observed in the pure anatase spectrum, which were assigned to the mica substrate. The corresponding modes for the rutile polymorph were found at 150 ($B_g$), 236, 444 ($E_g$) and 610 ($A_{1g}$) $cm^{-1}$. As expected, the characteristic Raman bands of the two polymorphs were also observed in the case of the single-shelled mix sample, although the anatase bands dominated the spectrum (Fig. 3(b)). It is worth noting that the double-shelled material showed anatase bands only and no traces of the rutile phase were detected. The fact that rutile was clearly observed in the XRD studies but untraceable in the Raman analysis of the double-shelled material is strong evidence of the full coverage of the particle by an homogeneous anatase $TiO_2$ overlayer.

The particle morphology was investigated by TEM. Fig. 4(a) shows a typical TEM image of the pure anatase sample, con-taining round particles within a range of sizes. The latter was attributed to the mica substrate. In contrast, the rutile coated particles seemed to crystallise/sinter into a hexagonal shape (Fig. 4(b)). Interestingly, the single-shelled mix material (Fig. 4(c)) combined features of both anatase and rutile particles, with a hexagonal structure clearly present but with rounded edges. Finally, the double-shelled particles, with the anatase phase deposited as an overlayer, showed very similar morphology to that of pure anatase (Fig. 4(d)), which supports the conclusions based on the Raman studies. A close inspection of the TEM images showed an apparently homogeneous coating of the mica substrate and no obvious imperfections or porosity could be observed. The thickness of the outer shell in the double-shelled sample, Fig. 4(d), was used to determine growth rates for the FBCVD process as ~1.7 nm $min^{-1}$. Whilst this growth rate seems low in comparison to normal CVD $TiO_2$ deposition processes, which are typically in the range of ~100 s nm $min^{-1}$, the former rate is expected once the surface area of the powder substrate is taken into account. The average particle size of the samples was estimated as 50–70 nm, in agreement with the crystallite size range estimated from the Scherrer equation (*vide supra*).

BET analysis was used to determine the surface areas of the samples, which ranged between 3–12 $m^2\ g^{-1}$ (Table 1), which is in accordance with literature values for similar sized $TiO_2$ particles.[51] These values are significantly lower than those for standard commercial powders, such as P25, with literature values of 56 $m^2\ g^{-1}$.[52] Interestingly, the BET results could be correlated with the particle sizes observed in the TEM images. The anatase and rutile nanoparticles had similar particle size and calculated surface areas, whilst the single-shelled mix sample contained small particles and large BET areas and the double-shelled material had the largest particles and correspondingly smallest area. The relatively low surface areas determined also suggested that the samples exhibited low porosity, giving further evidence of good surface coverage by the FBCVD route.

## Photodegradation of organic pollutants

The photocatalytic activity of the $TiO_2$-based samples synthesised in this work was assessed during mineralisation of

stearic acid, a model organic pollutant.[53] Stearic acid is very stable under UVA irradiation in the absence of a photocatalyst. The mineralisation of the acid can be formulated according to eqn (2) and it follows simple zero-order kinetics. The full mineralisation process requires 104 electrons.

$$CH_3(CH_2)_{16}CO_2H + 26O_2 \xrightarrow{TiO_2\left(h\nu \geq E_{bg}\right)} 18CO_2 + 18H_2O \quad (2)$$

The degradation of the acid can be easily monitored by FTIR, following the disappearance of C–H characteristic bands within the range of 2700–3000 $cm^{-1}$ (Fig. 5(a)). Typically, the degradation rates are estimated from linear regression of the initial 30–40% drop in integrated area of the acid characteristic IR-active bands. The degradation curves of stearic acid on the different $TiO_2$-based samples are shown in Fig. 5(b). The initial concentration of the acid did not change under the illumination conditions of the experiment (UVA, 4 ± 0.2 mW $cm^{-2}$) in the absence of a photocatalyst (on plain glass). The photocatalytic activity can be expressed as formal quantum efficiency ($\xi$), defined as molecules degraded per incident photon (molec $photon^{-1}$). The corresponding $\xi$ values are represented in Fig. 5(c). In this case, it was assumed that all incident photos were absorbed by the photocatalyst and they all had the same energy, corresponding to 365 nm ($E = 3.39$ eV). As expected in the case of photodegradation reactions of organic pollutants, the pure rutile sample showed negligible activity whilst the pure anatase sample showed the highest degradation rate (Fig. 5(c)).[54] The $\xi$ value of the anatase sample was consistent with those reported for thin films,[33] considering the thickness of the layers (≤100 nm) deposited in this work. The activity rates of the single- and double-shelled materials were found as intermediate between the pure rutile and anatase behaviours. The small difference in BET surface areas (3–12 $m^2\ g^{-1}$) was not considered relevant to the activity rates observed here (Table 1). The highest surface area was estimated for the anatase–rutile mix sample, however this sample did not show the highest activity. Similarly, both the double-shelled and pure anatase samples had similar surface areas (3 and 5 $m^2\ g^{-1}$, respectively) but the photocatalytic activity of the latter was significantly higher.

Inspection of the corresponding UV/vis spectra (Fig. 2) allowed correlation of their respective activities with the content of anatase and rutile phases in the single-shelled mix and double-shelled samples, provided any synergistic interaction between the polymorphs is ignored. However, the fact that the rutile–anatase systems showed poorer activities than that of pure anatase and anatase–rutile mix nanoparticles was surprising, since the synergistic interaction between the two $TiO_2$ polymorphs has been extensively reported.[33,55–58] It is important to highlight that the arrangement of the polymorphs in anatase–rutile systems should contribute to a vectorial separation of photogenerated charge pairs, as in a layered arrangement, and in any random anatase–rutile mixture the overall effect may be hindered.[35] When arranged appropriately, the anatase–rutile interaction contributes to an efficient charge separation and thus enhanced activity in these systems. The latter argument has been used to explain, for instance, the high photocatalytic efficiency of the commercial standard *Evonik* $TiO_2$ sample, formerly *Degussa P25*.[46] The mechanism of this interaction and in particular the band structure and electron transfer between the rutile and anatase phases is still a matter of debate. It has been generally accepted that rutile acts as an electron sink in anatase–rutile systems. However, evidence of electron transfer from rutile to anatase has been observed by EPR analysis.[56] The latter observation was also supported by recent calculations.[34] These authors suggested that the widely observed electron transfer from anatase to rutile is due to defects at the heterojunction level, which represent deep electron trap levels (1 eV below the conduction band) in rutile. This has been recently confirmed by transient spectroscopy studies on anatase–rutile mixtures which revealed hole transfer occurring from rutile to anatase.[59] This is relevant since it has been postulated that hydroxyl and hydroperoxyl radicals ($^{\bullet}OH$, $^{\bullet}O_2H$), formed in the reactions with participation of photogenerated holes and water molecules, are key species in the photodegradation of organic molecules.[60]

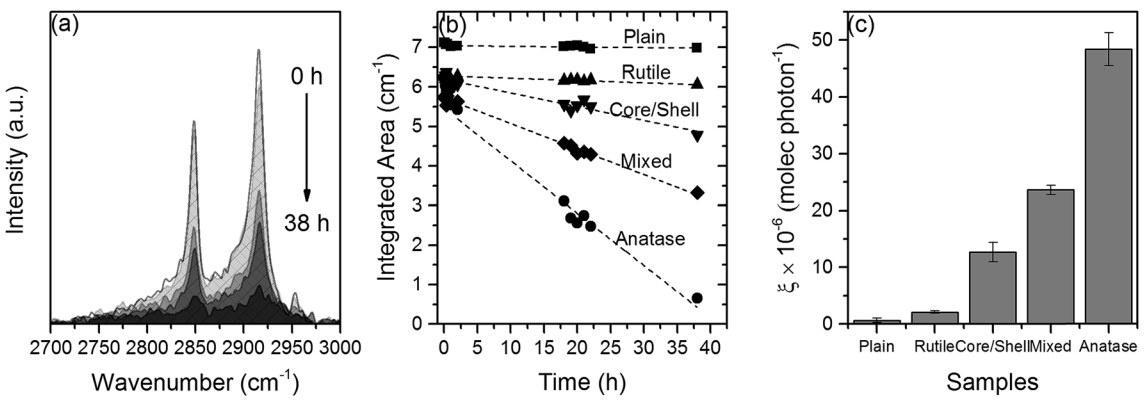


Fig. 5 (a) IR spectra of stearic acid during UVA illumination on $TiO_2$ anatase particles over 38 h. (b) Integrated areas of characteristic stearic acid IR-active bands (2700–3000 $cm^{-1}$) on rutile:anatase core–shell, anatase–rutile mixed-phase, pure rutile and pure anatase nanoparticles under UVA irradiation (4 ± 0.2 mW $cm^{-2}$). The integrated areas of the acid on plain glass (no catalyst) are included for reference. (c) Corresponding formal quantum efficiencies ($\xi$), defined as molecules of acid degraded per incident photon (molec $photon^{-1}$).

Here, the surprisingly low activity of the double-shelled sample could be due to the efficient coverage of the rutile layer by the deposition of the anatase overlayer, as inferred from the Raman results (Fig. 3(b)) and the discussion around the TEM/BET analysis. The exposure of both anatase and rutile phases to the medium also seems to play a crucial role in the activity enhancement observed for anatase–rutile samples. *Zhang et al.*[58] observed an enhanced activity of anatase-decorated rutile particles during $H_2$ evolution up to approximately 15 wt% anatase loading, but the activity of the samples dropped once the rutile phase was fully isolated from the medium. Similar observations were independently reported by *Kandiel et al.*,[55] for anatase-decorated rutile nanorods. The latter showed optimum photoactivity in the gas-phase degradation of acetaldehyde under UVA irradiation, however the nanorods became inactive once they were embedded in anatase nanoparticles. In the current work, an attempt was made towards the decoration of rutile components with anatase nanoparticles by changing the deposition times of the anatase phase (5, 10, 20 min). However, this approach resulted in homogeneous coatings with variable thicknesses and the activity of the resulting samples was similar to that of the double-shelled rutile@anatase material discussed here. In the case of the single-shelled mixed sample, its relatively high photoactivity could be explained considering that anatase will initially transform into rutile in the bulk of the particles, but the surface could still remain as anatase at the deposition temperature used in the synthesis (750 °C), according to previous studies in the literature.[58]

## Conclusions

A laboratory-scaled fluidised bed chemical vapour deposition (FBCVD) system has been introduced as an easily scalable, fast and cost effective route to produce multi-shelled and core–shell particles with the ability to tailor the core and shells to obtain desirable chemical properties. Single-shelled mix and double-shelled rutile@anatase $TiO_2$ particles were successfully synthesised and investigated as a case study. The $TiO_2$ shells were deposited on mica particles. The photocatalytic activity of these materials was studied during photodegradation of stearic acid. It was interesting to observe that the double-shelled rutile@anatase material showed a surprisingly low activity, which corroborates a number of reports that state both rutile and anatase polymorphs must be exposed to the medium for a photocatalytic efficiency enhancement in mixed-phase materials. This seemingly negative result is actually perceived as evidence for the coverage efficiency of the FBCVD method, as inferred from TEM, BET measurements and particularly Raman studies.

## Acknowledgements

Dr Andreas Kafizas is thanked for discussion on rutile–anatase interaction and Martin Vickers and Diana Teixeira Gómez for access and acquisition of XRD patterns.

## Notes and references

1 W. Ye, M. F. Leung, J. Xin, T. L. Kwong, D. K. L. Lee and P. Li, *Polymer*, 2005, **46**, 10538–10543.
2 H. Sakai, T. Kanda, H. Shibata, T. Ohkubo and M. Abe, *J. Am. Chem. Soc.*, 2006, **128**, 4944–4945.
3 B. Chudasama, A. K. Vala, N. Andhariya, R. Upadhyay and R. Mehta, *Nano Res.*, 2009, **2**, 955–965.
4 V. Salgueiriño-Maceira and M. A. Correa-Duarte, *Adv. Mater.*, 2007, **19**, 4131–4144.
5 D. V. Talapin, I. Mekis, S. Götzinger, A. Kornowski, O. Benson and H. Weller, *J. Phys. Chem. B*, 2004, **108**, 18826–18831.
6 Z. Xu, Y. Hou and S. Sun, *J. Am. Chem. Soc.*, 2007, **129**, 8698–8699.
7 K. Maeda, K. Teramura, D. Lu, N. Saito, Y. Inoue and K. Domen, *Angew. Chem.*, 2006, **118**, 7970–7973.
8 S. Shanmugam, A. Gabashvili, D. S. Jacob, J. C. Yu and A. Gedanken, *Chem. Mater.*, 2006, **18**, 2275–2282.
9 X. W. Wang, G. Liu, G. Q. Lu and H. M. Cheng, *Int. J. Hydrogen Energy*, 2010, **35**, 8199–8205.
10 S.-Y. Li, G. A. Niklasson and C.-G. Granqvist, *J. Appl. Phys.*, 2011, **109**, 113515.
11 Y. Gao, S. Wang, H. Luo, L. Dai, C. Cao, Y. Liu, Z. Chen and M. Kanehira, *Energy Environ. Sci.*, 2012, **5**, 6104–6110.
12 Y. Li, S. Ji, Y. Gao, H. Luo and M. Kanehira, *Sci. Rep.*, 2013, **3**, 1370.
13 B. Dabbousi, J. Rodriguez-Viejo, F. V. Mikulec, J. Heine, H. Mattoussi, R. Ober, K. Jensen and M. Bawendi, *J. Phys. Chem. B*, 1997, **101**, 9463–9475.
14 S. Kim, B. Fisher, H.-J. Eisler and M. Bawendi, *J. Am. Chem. Soc.*, 2003, **125**, 11466–11467.
15 D. Valerini, A. Creti, M. Lomascolo, L. Manna, R. Cingolani and M. Anni, *Phys. Rev. B: Condens. Matter Mater. Phys.*, 2005, **71**, 235409.
16 L.-F. Cui, R. Ruffo, C. K. Chan, H. Peng and Y. Cui, *Nano Lett.*, 2008, **9**, 491–495.
17 M. Ren, Z. Zhou, X. Gao, W. Peng and J. Wei, *J. Phys. Chem. C*, 2008, **112**, 5689–5693.
18 B. Sun, Z. Chen, H.-S. Kim, H. Ahn and G. Wang, *J. Power Sources*, 2011, **196**, 3346–3349.
19 J. Liu, J. Jiang, C. Cheng, H. Li, J. Zhang, H. Gong and H. J. Fan, *Adv. Mater.*, 2011, **23**, 2076–2081.
20 X. Xia, J. Tu, Y. Zhang, X. Wang, C. Gu, X.-B. Zhao and H. J. Fan, *ACS Nano*, 2012, **6**, 5531–5538.
21 P. Yang, X. Xiao, Y. Li, Y. Ding, P. Qiang, X. Tan, W. Mai, Z. Lin, W. Wu and T. Li, *ACS Nano*, 2013, **7**, 2617–2626.
22 C.-H. Tang, X. Yin and H. Gong, *ACS Appl. Mater. Interfaces*, 2013, **5**, 10574–10582.
23 D. Liu, Y. Gao, D. Gao and X. Han, *Opt. Commun.*, 2012, **285**, 1988–1992.
24 F. Wang, R. Deng, J. Wang, Q. Wang, Y. Han, H. Zhu, X. Chen and X. Liu, *Nat. Mater.*, 2011, **10**, 968–973.
25 K. L. Choy, *Prog. Mater. Sci.*, 2003, **48**, 57–170.
26 T. D. Manning, I. P. Parkin, R. J. H. Clark, D. Sheel, M. E. Pemble and D. Vernadou, *J. Mater. Chem.*, 2002, **12**, 2936–2939.

27 S. A. O'Neill, I. P. Parkin, R. J. Clark, A. Mills and N. Elliott, *J. Mater. Chem.*, 2003, **13**, 56–60.
28 A. Mills, A. Lepre, N. Elliott, S. Bhopal, I. P. Parkin and S. O'neill, *J. Photochem. Photobiol., A*, 2003, **160**, 213–224.
29 S. Kinkel, G. Angelopoulos and W. Dahl, *Surf. Coat. Technol.*, 1994, **64**, 119–125.
30 R. Moene, L. Kramer, J. Schoonman, M. Makkee and J. Moulijn, *Appl. Catal., A*, 1997, **162**, 181–191.
31 N. Voudouris, C. Christoglou and G. Angelopoulos, *Surf. Coat. Technol.*, 2001, **141**, 275–282.
32 F. Danafar, A. Fakhru'l-Razi, M. A. M. Salleh and D. R. A. Biak, *Chem. Eng. J.*, 2009, **155**, 37–48.
33 R. Quesada-Cabrera, C. Sotelo-Vazquez, J. C. Bear, J. A. Darr and I. P. Parkin, *Adv. Mater. Interfaces*, 2014, **1**, 1400069.
34 D. O. Scanlon, C. W. Dunnill, J. Buckeridge, S. A. Shevlin, A. J. Logsdail, S. M. Woodley, C. R. A. Catlow, M. J. Powell, R. G. Palgrave and I. P. Parkin, *Nat. Mater.*, 2013, **12**, 798–801.
35 A. Kafizas, C. J. Carmalt and I. P. Parkin, *Chem.–Eur. J.*, 2012, **18**, 13048–13058.
36 S. Jun, E. Jang and J. E. Lim, *Nanotechnology*, 2006, **17**, 3892.
37 X. Li, D. Shen, J. Yang, C. Yao, R. Che, F. Zhang and D. Zhao, *Chem. Mater.*, 2012, **25**, 106–112.
38 L. M. Liz-Marzán, M. Giersig and P. Mulvaney, *Langmuir*, 1996, **12**, 4329–4335.
39 Y. Lu, Y. Yin, Z.-Y. Li and Y. Xia, *Nano Lett.*, 2002, **2**, 785–788.
40 J. Lee, J. C. Park and H. Song, *Adv. Mater.*, 2008, **20**, 1523–1528.
41 T. D. Manning, I. P. Parkin, M. E. Pemble, D. Sheel and D. Vernardou, *Chem. Mater.*, 2004, **16**, 744–749.
42 H. M. Yates, M. G. Nolan, D. W. Sheel and M. E. Pemble, *J. Photochem. Photobiol., A*, 2006, **179**, 213–223.
43 A. Kafizas, C. Crick and I. P. Parkin, *J. Photochem. Photobiol., A*, 2010, **216**, 156–166.
44 A. Kafizas, C. W. Dunnill and I. P. Parkin, *J. Mater. Chem.*, 2010, **20**, 8336–8349.
45 S. A. O'Neill, R. J. Clark, I. P. Parkin, N. Elliott and A. Mills, *Chem. Mater.*, 2003, **15**, 46–50.
46 B. Ohtani, O. Prieto-Mahaney, D. Li and R. Abe, *J. Photochem. Photobiol., A*, 2010, **216**, 179–182.
47 J. Tauc, *Mater. Res. Bull.*, 1968, **3**, 37–46.
48 H. Tang, K. Prasad, R. Sanjines, P. Schmid and F. Levy, *J. Appl. Phys.*, 1994, **75**, 2042–2047.
49 M. Batzill, E. H. Morales and U. Diebold, *Phys. Rev. Lett.*, 2006, **96**, 026103.
50 U. Balachandran and N. Eror, *J. Solid State Chem.*, 1982, **42**, 276–282.
51 M. Anpo, T. Shima, S. Kodama and Y. Kubokawa, *J. Phys. Chem.*, 1987, **91**, 4305–4310.
52 K. J. A. Raj and B. Viswanathan, *Indian J. Chem., Sect. A: Inorg., Bio-inorg., Phys., Theor. Anal. Chem.*, 2009, **48**, 1378.
53 A. Mills and J. S. Wang, *J. Photochem. Photobiol., A*, 2006, **182**, 181–186.
54 H. Kominami, S.-Y. Murakami, J.-I. Kato, Y. Kera and B. Ohtani, *J. Phys. Chem. B*, 2002, **106**, 10501–10507.
55 T. A. Kandiel, R. Dillert, A. Feldhoff and D. W. Bahnemann, *J. Phys. Chem. C*, 2010, **114**, 4909–4915.
56 D. C. Hurum, A. G. Agrios, K. A. Gray, T. Rajh and M. C. Thurnauer, *J. Phys. Chem. B*, 2003, **107**, 4545–4549.
57 T. Ohno, K. Tokieda, S. Higashida and M. Matsumura, *Appl. Catal., A*, 2003, **244**, 383–391.
58 J. Zhang, Q. Xu, Z. Feng, M. Li and C. Li, *Angew. Chem., Int. Ed.*, 2008, **47**, 1766–1769.
59 X. Wang, A. Kafizas, X. Li, S. J. A. Moniz, P. J. T. Reardon, J. Tang, I. P. Parkin and J. R. Durrant, *J. Phys. Chem. C*, 2015, **119**(19), 10439–10447.
60 M. R. Hoffmann, S. T. Martin, W. Choi and D. W. Bahnemann, *Chem. Rev.*, 1995, **95**, 69–96.